Green Chemical Technology

SCIEPublish

Article

Solar−Driven Antibiotic Ciprofloxacin Elimination by $Bi_4Ti_3O_{12}$ and Biotoxicity Evaluation of Degradation Process on Aquatic Organisms and Bean Seedling

Bingwen Hu, Kefan Chen, Jialiang Wu and Gang Cheng *

School of Chemistry and Environmental Engineering, Wuhan Institute of Technology, Donghu New & High Technology Development Zone, Wuhan 430205, China; bingwenh@163.com (B.H.); 18942199406@163.com (K.C.); wjl3267436120@163.com (J.W.)

* Corresponding author. E-mail: gchenglab@163.com or gcheng@wit.edu.cn (G.C.)

Received: 5 March 2026; Revised: 2 April 2026; Accepted: 11 May 2026; Available online: 18 May 2026

ABSTRACT: Photocatalytic degradation of antibiotic molecules has great significance in environmental pollution control. $Bi_4Ti_3O_{12}$ with a layered structure is one of the emerging visible−light−responsive photocatalysts. However, the environmental effects of antibiotic degradation have not received sufficient attention. This study employed plate−like $Bi_4Ti_3O_{12}$ derived from $Na_2Ti_3O_7$ nanowires for ciprofloxacin (CIP) degradation, and investigated the biotoxicity of degradation products on aquatic organisms and plant seedlings. It was found that an appropriate hydrothermal treatment time with ethylene glycol could slightly enhance the photocatalytic performance of $Bi_4Ti_3O_{12}$, and this might be attributed to the increased density of active sites resulting from the regulation of microstructure. Concurrently, the degradation products of CIP were detected and predicted for biotoxicity; the effects of the CIP degradation residual solution on the growth of peas, wheat, and zebrafish larvae were also investigated. Under the present experimental conditions, the $Bi_4Ti_3O_{12}$−24h photocatalyst−involved CIP degradation process could reduce the biotoxicity of the CIP solution (40 mg/L) and exhibit low toxicity to several individual organisms, including some actual plants and animals.

Keywords: Photocatalysis; Antibiotics; $Bi_4Ti_3O_{12}$; Degradation process; Biotoxicity

1. Introduction

Since the social industrialization, the human living environment has been severely polluted, with numerous highly toxic, teratogenic, and carcinogenic substances entering the environment through wastewater discharge. The antibiotic ciprofloxacin (CIP), with excellent antibacterial properties, has been widely used in medical treatment and animal husbandry [1]. However, the study pointed out that only a small portion of CIP could be absorbed and metabolized after intake by animals [2]. The majority would be excreted as drug prototypes or primary metabolites [3]. This would lead to long−term exposure of microorganisms and animals to the CIP environment, thereby accelerating the emergence of antibiotic-

© 2026 The authors. This is an open access article under the Creative Commons Attribution 4.0 International License (https://creativecommons.org/licenses/by/4.0/).

resistant bacteria [4]. Meanwhile, CIP might accumulate in the human body through the food chain, disrupting the human nervous and endocrine systems [5,6]. Therefore, efficiently and environmentally removing antibiotics is an unavoidable challenge for humanity in protecting our living environment.

However, traditional physical separation techniques and biodegradation methods struggle to achieve complete removal of antibiotics [7]. Solar energy, a green, safe, and widely available renewable resource, has been extensively studied for utilization in recent decades [8,9], including organic synthesis, hydrogen production, plastic upcycling, pollutant removal, *etc*. [10–12]. Among these technologies, semiconductor photocatalysis attracts significant attention for addressing environmental pollution. Powered by solar energy, generating free radicals under mild reaction conditions to mineralize organic pollutants into non−toxic small−molecule products, thereby reducing the secondary pollution risk [13–15]. However, it should be noted that most current research focuses on the design and development of highly efficient photocatalysts to achieve rapid pollutant removal. Only a few studies predict the toxicity variation during the degradation process, and researchers often overlook whether the parent compounds might undergo biomagnification to produce higher−toxicity degradation products. According to relevant reports [16], approximately 44% of studies reported that wastewater toxicity decreased after photocatalytic treatment. Li et al. [17] observed during the degradation of norfloxacin that most mineralized products increased the acute toxicity of the photocatalytic reaction solution, and further introduction of microalgae reduced the toxicity of the reaction solution. Tošić et al. [18] confirmed that although photodegradation achieved over 90% degradation of carbofuran, the residual solution remained toxic to cells. Moreover, the toxicity of degradation products to wheat seedlings increased with degradation duration. Therefore, it is not sufficient to evaluate the toxicity of the reaction solution solely based on the removal of parent compounds during the photocatalytic elimination of organic pollutants. The toxicity of intermediate products must also be evaluated to ensure no new hazards are introduced to the environment. This is especially critical when organic substances are not completely mineralized, making biological toxicity assessment particularly important.

It is generally known that the key to photocatalytic technology lies in the photocatalyst. In recent years, bismuth titanate−based semiconductor photocatalysts have demonstrated significant potential for environmental remediation due to their appropriate bandgap and high photothermal stability [19]. Among these, perovskite bismuth titanate ($Bi_4Ti_3O_{12}$) formed by alternating stacks of $[Bi_2O_2]^{2+}$ layers and $[Bi_2Ti_3O_{10}]^{2-}$ layers along the *c*−axis facilitates photocatalytic reactions primarily within the interlayer space [20]. This unique layered structure promotes efficient separation of photogenerated electrons and holes [21–23]. As with other semiconductors, rapid recombination of holes and electrons persists in both the bulk and the surface of $Bi_4Ti_3O_{12}$, resulting in low catalytic activity that is insufficient for practical applications. Therefore, how to enhance the photocatalytic activity of $Bi_4Ti_3O_{12}$ remains a hot topic of current research. To present, various strategies have been identified to enhance the catalytic activity of $Bi_4Ti_3O_{12}$, such as constructing heterojunctions, metal ion doping, non−metal ion doping, and noble metal deposition [24–27]. However, researchers have demonstrated that simple thermal treatment of certain semiconductors can improve their photocatalytic performance. For example, Wan et al. [28] subjected anatase TiO_2 nanoparticles to ethylene glycol thermal treatment, resulting in a twofold increase in the hydrogen production rate under visible light irradiation. Gao et al. [29] thermally treated TiO_2 nanotube arrays coated with aluminum powder; surface defects formed during calcination optimized the photoinduced charge behavior, and hydrogen release rates from the modified black TiO_2 increased 12−fold. In recent years, most of the reports on the organic pollutants removal using $Bi_4Ti_3O_{12}$ photocatalysts mainly focused on dyes (e.g., rhodamine B) and tetracycline hydrochloride antibiotics [21,22,30]; there were few works relevant to the degradation of CIP and the toxicity of CIP degradation products.

Based on the above background, this study employed $Na_2Ti_3O_7$ as a precursor to synthesize $Bi_4Ti_3O_{12}$ via the hydrothermal method. Subsequently, the structure of $Bi_4Ti_3O_{12}$ was optimized through hydrothermal treatment with ethylene glycol. CIP degradation tests were conducted to evaluate the impact of different

post−treatment durations on the catalytic performance of $Bi_4Ti_3O_{12}$. The impact of ethylene glycol treatment on $Bi_4Ti_3O_{12}$ photocatalytic performance was analyzed by incorporating morphological characteristics, physicochemical properties, and photoelectrochemical characterization. Finally, the study investigated the biotoxicity of the CIP degradation products to aquatic organisms and the toxicity effects of the degradation residual solution on some actual plants and animals.

2. Experimental Section

2.1. Material Synthesis

The precursor $Na_2Ti_3O_7$ was synthesized via a one−step hydrothermal method. 32 g of NaOH were dissolved in 70 mL of deionized water. Then, 2.4 g of TiO_2 particles were added to the solution, dispersed by ultrasonication, and stirred for 30 min. The mixture was transferred to a 100 mL Teflon−lined autoclave and kept at 180 ℃ for 24 h. After cooling to room temperature, the white solid was washed several times with deionized water and alcohol, then drying at 120 ℃ in an oven for 12 h to obtain $Na_2Ti_3O_7$. As previously reported [31], $Bi_4Ti_3O_{12}$ nanosheet structures were synthesized via hydrothermal synthesis of Bi^{3+} and $Na_2Ti_3O_7$ in a strongly alkaline environment. Typically, 0.97 g of $Bi(NO_3)_3{\cdot}5H_2O$ was dispersed in 70 mL of NaOH solution (3 mol/L), then added 0.15 g of $Na_2Ti_3O_7$. After stirring for 30 min, the mixture was transferred to 100 mL Teflon−lined autoclave and reacted at 180 ℃ for 24 h. The pale−yellow solid obtained was washed several times with deionized water and once with ethanol, then dried under vacuum at 60 ℃ for 12 h to yield $Bi_4Ti_3O_{12}$. Finally, 0.3 g of $Bi_4Ti_3O_{12}$ was ultrasonically dispersed in a mixture of 30 mL ethylene glycol and 30 mL deionized water and stirred for 30 min, then transferred to a Teflon−lined autoclave and kept at 120 ℃ for 12 h. The suspension was then centrifuged and washed several times with deionized water until the pH was natural, dried at 60 ℃ for 12 h, and denoted as $Bi_4Ti_3O_{12}$−12h. The reaction times of 24 and 36 h are denoted as $Bi_4Ti_3O_{12}$−24h and $Bi_4Ti_3O_{12}$−36h, respectively. The schematic diagram of material synthesis is shown in Figure 1.

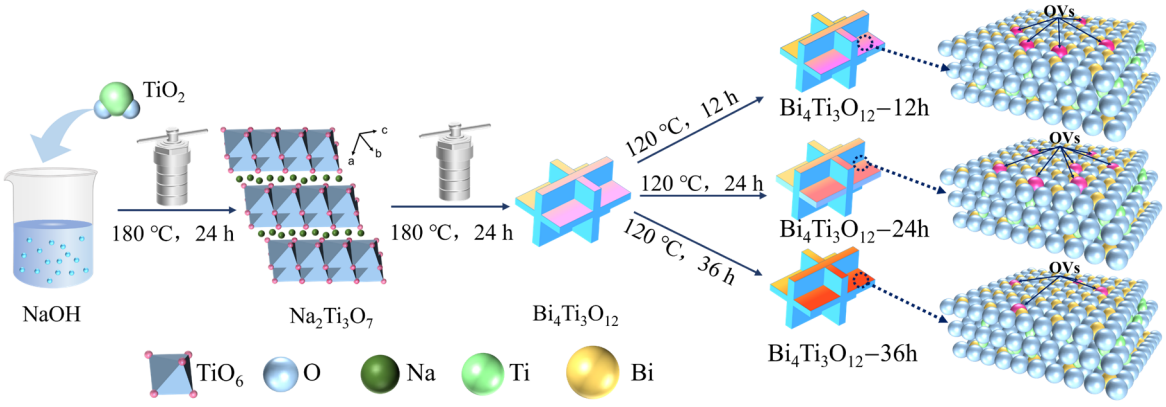

Figure 1. Synthesis schematic of $Bi_4Ti_3O_{12}$ nanosheets derived from $Na_2Ti_3O_7$ nanowires as precursor.

2.2. Materials Characterization

The composition, structure, properties, and other characteristics of the prepared materials were detailed in the Supplementary Materials.

2.3. Photocatalytic Degradation Test

The 10 mg of prepared $Bi_4Ti_3O_{12}$, $Bi_4Ti_3O_{12}$−12h, $Bi_4Ti_3O_{12}$−24h, and $Bi_4Ti_3O_{12}$−36h photocatalysts were dispersed in freshly prepared CIP solution and ultrasonically homogenized. Dark adsorption was performed 1 h before irradiation to achieve adsorption–desorption equilibrium between the catalyst and CIP molecules. Subsequently, the photocatalytic degradation was conducted using a 300 W Xe lamp to

simulate sunlight. At certain intervals, 3 mL of the suspension was collected and centrifuged. Finally, the absorbance of the supernatant was measured using a UV spectrophotometer (UV−PC 1900) at λ = 276 nm. The photocatalytic performance differences were evaluated by calculating the ratios C_t/C_0 and $-\ln(C_t/C_0)$ and plotting the corresponding curves. It should be noted that interference induced by degradation products could not be fully excluded during absorbance measurement, therefore may be certain deviations between the actual removal efficiency and the calculated efficiency.

2.4. Biotoxicity Assessment of CIP Degradation Residual Solution

Regarding plant toxicity, uniformly sized, plump pea and wheat seeds were divided equally into three groups. After soaking in water for 12 h, the seeds were placed in planting baskets. The seedlings were sprayed with deionized water, CIP solution (40 mg/L), and CIP degradation residual solution (irradiation for 4 h) at intervals of 4 h to promote germination and growth. The toxicity effects of each solution on the seedlings were assessed by observing the growth behavior of the seedlings daily.

In terms of animal toxicity, the newly hatched zebrafish larvae were purchased from an aquarium, and then acclimatized in deionized water for 6 h. After that, the same number of larvae with consistent vitality were placed in deionized water, in CIP degradation residual solution (irradiated for 2 or 4 h), and in CIP solution (40 mg/L). The solution in each group was renewed every 12 h. The growth differences among larvae in each group were recorded as a basis for evaluating the biological toxicity of different solutions to zebrafish.

3. Results and Discussion

The composition of the prepared materials was characterized by XRD. Figure 2a reveals that the characteristic peaks of the as prepared $Na_2Ti_3O_7$ correspond to the standard card (JCPDS No. 31−1329). Although some characteristic peaks of the $Na_2Ti_3O_7$ sample are lower in intensity, no impurity peaks appear, indicating high purity of the sample. Figure 2b shows the XRD patterns of the $Bi_4Ti_3O_{12}$, $Bi_4Ti_3O_{12}$−12h, $Bi_4Ti_3O_{12}$−24h, and $Bi_4Ti_3O_{12}$−36h. All synthetic products are well indexed by the standard XRD pattern of $Bi_4Ti_3O_{12}$ (JCPDS No. 89−7500), confirming the synthesis of $Bi_4Ti_3O_{12}$ via the hydrothermal method. Surface morphology and structure of the prepared materials were characterized using scanning electron microscopy (SEM). Figure 2c,d reveals that the $Na_2Ti_3O_7$ sample exhibits a nanowire−like structure. Figure 2e shows that $Bi_4Ti_3O_{12}$ exhibits a sphere−like structure formed by the cross−assembly of regular nanosheets, which may be attributed to the large surface energy [32]. Meanwhile, Figure 2f–h exhibits that $Bi_4Ti_3O_{12}$ after heat treatment remains a comparable microstructure, indicating that low−temperature heat treatment struggles to alter the overall structure of $Bi_4Ti_3O_{12}$. Nevertheless, it can be observed that partial fragmentation of nanosheets occurs on the $Bi_4Ti_3O_{12}$ surface upon extended hydrothermal treatment time with ethylene glycol, which may be attributed to excessive heat treatment disrupting the internal layered structure.

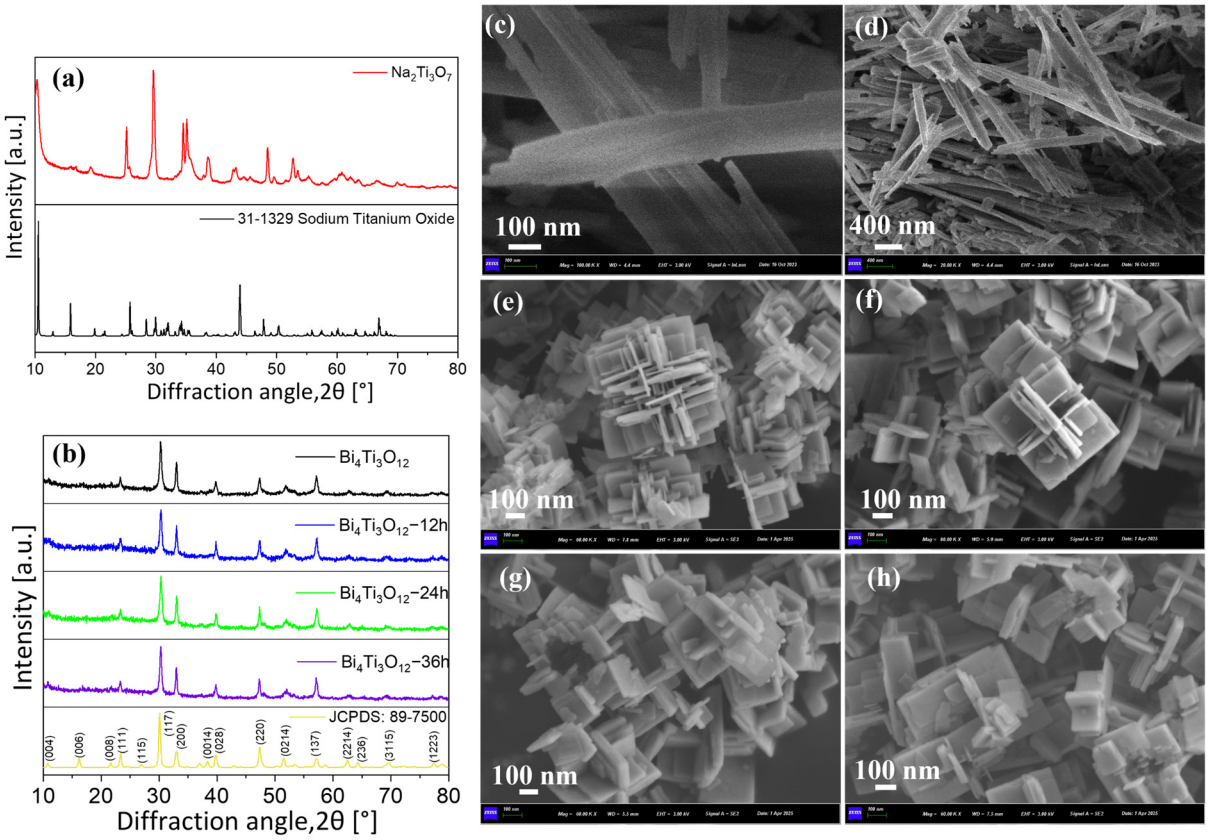

Figure 2. XRD patterns of $Na_2Ti_3O_7$ (**a**) and $Bi_4Ti_3O_{12}$ (**b**); SEM image of $Na_2Ti_3O_7$ (**c**,**d**), $Bi_4Ti_3O_{12}$ (**e**), $Bi_4Ti_3O_{12}$−12h (**f**), $Bi_4Ti_3O_{12}$−24h (**g**), $Bi_4Ti_3O_{12}$−36h (**h**).

The CIP solution was degraded under dark and light conditions to evaluate the effectiveness of photocatalytic pollutant removal. Figure 3a shows the A_t/A_0 versus time curves for the catalytic degradation of CIP solution (50 mL, 40 mg/L) for four samples, in which A_t represents the residual absorbance of the CIP solution at different degradation times, and A_0 denotes the initial one. Notably, CIP molecules were not decomposed under light irradiation alone, indicating that CIP degradation was catalytically induced. As can be seen, the photocatalytic activity of the four samples followed the order: $Bi_4Ti_3O_{12}$−24h > $Bi_4Ti_3O_{12}$−12h > $Bi_4Ti_3O_{12}$ > $Bi_4Ti_3O_{12}$−36h. Thus, treating $Bi_4Ti_3O_{12}$ with ethylene glycol for an appropriate duration could slightly enhance photocatalytic performance. Figure 3b shows the first−order kinetic curves. Similarly, the sample $Bi_4Ti_3O_{12}$−24h exhibited the fastest degradation rate for CIP, attaining $k = 0.00245$ min^{-1}. In particular, as shown in Table S1, the photocatalytic degradation rate of $Bi_4Ti_3O_{12}$−24h is higher than that of some previously reported photocatalysts. Figure S1–S3 present the degradation curves and first−order kinetic curves of the four samples toward CIP solutions at equal concentration gradients. The order of photocatalytic activity among the four samples aligns with that shown in Figure 3a,b. $Bi_4Ti_3O_{12}$−24h achieved a degradation rate of 67% for the CIP solution (10 mg/L), as well as a decrease in degradation rate with increasing CIP solution concentration. Figure 3c shows the investigation of optimal active species in the photocatalytic process of $Bi_4Ti_3O_{12}$−24h utilizing active species scavengers. In this case, isopropyl alcohol (IPA), nitrogen (N_2), methanol, and CCl_4 remove ·OH, $\cdot O_2^-$, h^+, and e^-, respectively [33]. It was found that the degradation curve decreased upon addition of any scavenger compared to the initial conditions, indicating that multiple active species were involved in the CIP degradation process. However, the addition of IPA showed the most significant decrease in the curve, demonstrating that ·OH may have played an important role in the catalytic process. As shown in Figure 3d, the CIP degradation rate constants for various scavengers further corroborated this point.

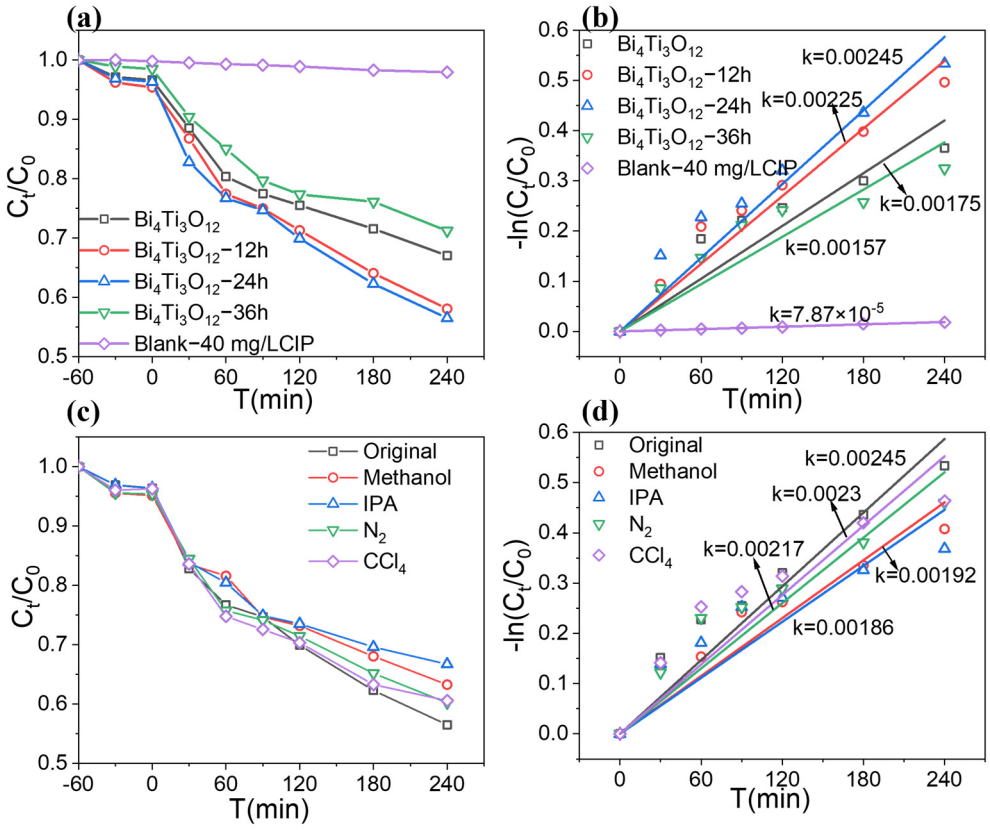

Figure 3. (**a**) Degradation curves and (**b**) kinetic curves of CIP with different catalysts; (**c**) degradation curves and (**d**) kinetic curves of CIP in the presence of different scavengers.

To gain a deeper understanding of the photogenerated carrier separation efficiency of the prepared materials, photo− and electrochemical measurements were performed on $Bi_4Ti_3O_{12}$, $Bi_4Ti_3O_{12}$−12h, $Bi_4Ti_3O_{12}$−24h, and $Bi_4Ti_3O_{12}$−36h. Typically, the higher photocurrent response signal improved h^+ and e^- separation efficiency [34,35]. As shown in Figure 4a, the magnitude of the current generated by the electrode was evaluated using photocurrents (PC) under irradiation conditions. When the test light source was turned on or off, the sample $Bi_4Ti_3O_{12}$−24h exhibited the highest photocurrent signal compared to pristine $Bi_4Ti_3O_{12}$, suggesting that charge separation is likely improved [36]. It was further verified by electrochemical impedance spectroscopy (EIS). Figure 4b displays the Nyquist plot of the EIS test, where the magnitude of resistance encountered during charge transfer is inversely proportional to the circle radius [37,38]. The sample $Bi_4Ti_3O_{12}$−24h exhibited the smallest circle radius and the highest charge−transfer efficiency. Additionally, the electrochemical activity of the catalysts was evaluated using linear sweep voltammetry (LSV), as illustrated in Figure 4c. At the same test voltage, the $Bi_4Ti_3O_{12}$−24h exhibited the lowest cathodic current density, indicating superior activity during the reduction process [39,40]. To investigate the effect of active sites on the photocatalytic performance of the catalyst surface, the electrochemically active area was evaluated by cyclic voltammetry (CV). Typically, the double−layer capacitance of the sample was calculated by fitting the CV curve, and the number of active sites could be estimated [41,42]. Figure S4a–d shows the double−layer capacitance of samples $Bi_4Ti_3O_{12}$, $Bi_4Ti_3O_{12}$−12h, $Bi_4Ti_3O_{12}$−24h, and $Bi_4Ti_3O_{12}$−36h at different scan rates (10–100 $mV \cdot s^{-1}$). And then these curves were fitted to yield straight lines, with the slope *k* representing the double−layer capacitance, as shown in Figure 4d. After thermal treatment with ethylene glycol for an appropriate duration, the number of active sites in $Bi_4Ti_3O_{12}$ significantly increased. Therefore, the photocatalytic activity of $Bi_4Ti_3O_{12}$−24h may be closely related to the increased number of active sites. Figure S5a,b presents the UV−visible diffuse reflectance spectroscopy (UV−vis DRS) and Tauc plots of the as−prepared materials. Interestingly, hydrothermal

treatment with ethylene glycol did not modify the photo−absorption range and bandgap width of $Bi_4Ti_3O_{12}$ [43]. Concurrently, in Figure S6, the EPR test results for the samples also indicated that ethylene glycol struggled to effectively induce the generation of oxygen vacancies on the $Bi_4Ti_3O_{12}$ surface [44]. The above findings showed that selecting an appropriate duration for ethylene glycol heat treatment could optimize the separation behavior of photogenerated carriers and increase the number of active sites. However, excessive treatment may disrupt the layered crystal lattice structure of $Bi_4Ti_3O_{12}$, leading to a broken migration pathway for photogenerated carriers and lower catalytic performance. Figure 4e illustrates the photocatalytic degradation of CIP by $Bi_4Ti_3O_{12}$.

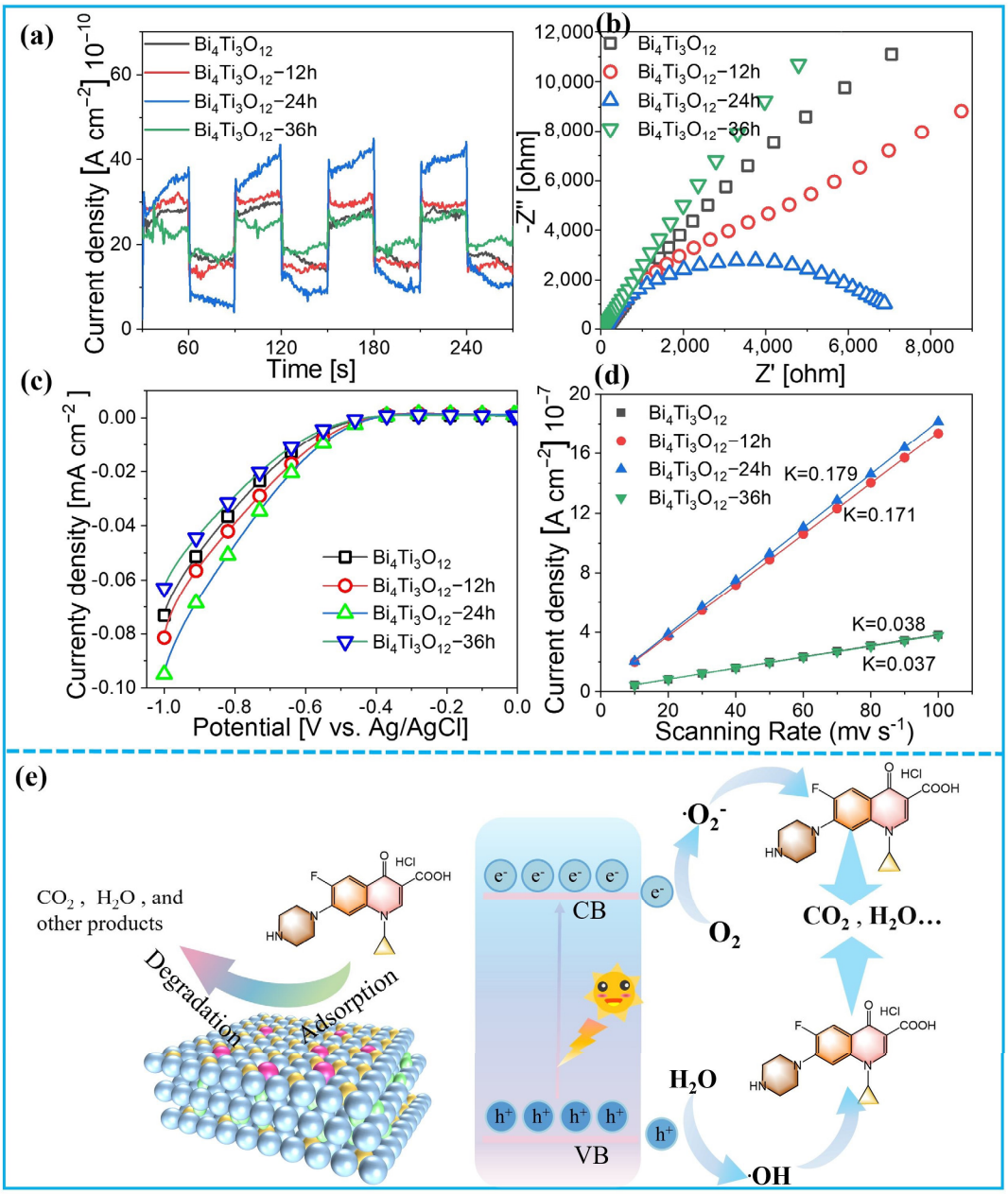

Figure 4. (**a**) PC; (**b**) EIS; (**c**) LSV; and (**d**) CV of $Bi_4Ti_3O_{12}$, $Bi_4Ti_3O_{12}$−12h, $Bi_4Ti_3O_{12}$−24h, and $Bi_4Ti_3O_{12}$−36h; (**e**) CIP degradation schematic diagram.

To guarantee the investigation of the biological toxicity of CIP degradation intermediates, high−resolution mass spectrometry (HRMS) was employed to characterize the degradation products [45,46]. Figure S7a–c shows the spectra of degradation time at 30, 120, and 240 min, respectively, and eight major intermediate products were tentatively identified during

the degradation process. It should be noted that the structural formulas of the intermediates were only tentative, based entirely on mass spectrometry data (m/z values and fragmentation patterns) and had not been confirmed by other techniques. Relevant studies have revealed that the formation of intermediates in the photooxidation process of CIP typically begins with the cleavage of the piperazine ring and the elimination of the carboxyl group [47,48]. The oxidation process primarily involves defluorination, decarboxylation, and the opening of the cyclic structure. According to the structure of the intermediate products, two possible degradation pathways of CIP have been proposed, as illustrated in Figure 5. First, in pathway I, the piperazine ring in CIP underwent oxidation by ·OH, opening the ring structure to form the monoaldehyde derivative P1 [49]. Subsequently, upon decarboxylation, defluorination, and unstable piperazine ring cleavage, P1 was converted to P2. With further action from reactive species, the quinolone ring underwent cleavage to open the ring structure, yielding multiple small−molecule products. In pathway II, the piperazine ring in CIP was directly fractured after cleavage to form an unstable intermediate, then oxidation of the carboxyl group produces P6 [50]. P7 was formed when P6 was degraded via the quinolone ring and cyclopropyl group, completely losing the carboxyl group. Afterward, the aromatic ring structure was cleaved, yielding intermediate P8 [51]. Ultimately, these small−molecule intermediates, P3, P4, P5, and P8, were quite likely to be decomposed into CO_2, H_2O, and other products.

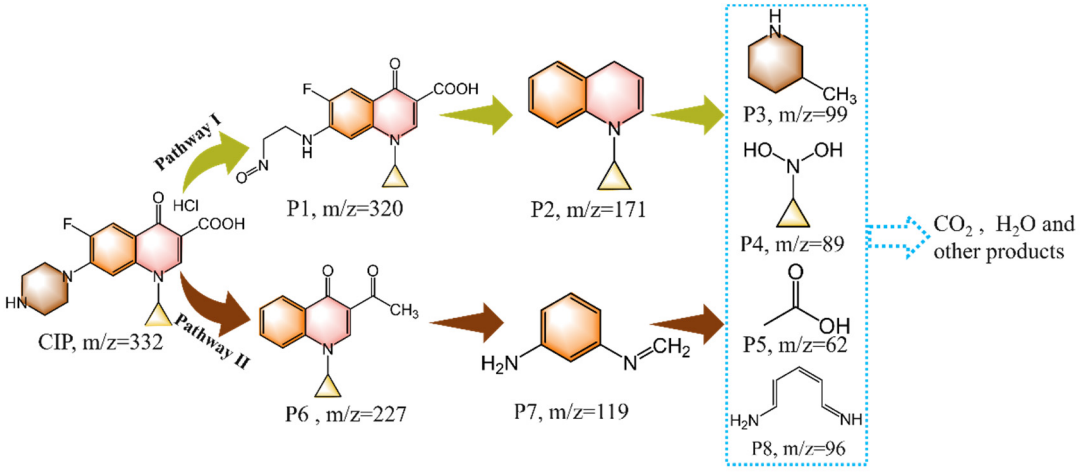

Figure 5. Possible degradation pathways of CIP upon $Bi_4Ti_3O_{12}$−24h.

To gain a deeper insight into the biological toxicity of CIP and degradation products, the Ecological Structure−Activity Relationship (ECOSAR) prediction model was employed to evaluate their toxicity levels toward aquatic organisms (fish, Daphnia, and green algae) [52–54]. The toxicity assessment of these chemicals adhered to the guidelines for chemical hazard evaluation established by China. As shown in Figure 6, CIP and most intermediates were predicted to have relatively high toxicity thresholds for aquatic organisms, but still generated some more toxic intermediates. For instance, intermediate P2 was predicted to exhibit acute and chronic toxicity to all three aquatic organisms. Regarding chronic toxicity, P3 and P7 were highly toxic to daphnia, with LC_{50} values of 0.3 and 0.03 mg/L, respectively, which were significantly below the toxicity standard (10 mg/L) and posed a substantial threat to aquatic survival. Therefore, to achieve green emission requirements, it is crucial to either deeply treat the reaction solution or further upgrade the catalyst. However, it should be noted that ECOSAR is a quantitative structure−activity relationship (QSAR)−based predictive model and the results represent theoretical estimates rather than experimentally determined toxicity values. It is not sufficient to rely solely on a predictive model to determine the toxicity of the CIP degradation process. Actual concentrations of toxic intermediates during degradation, as well as the actual environmental toxicity of the reaction solution under the combined effects of multiple substances, must also be considered.

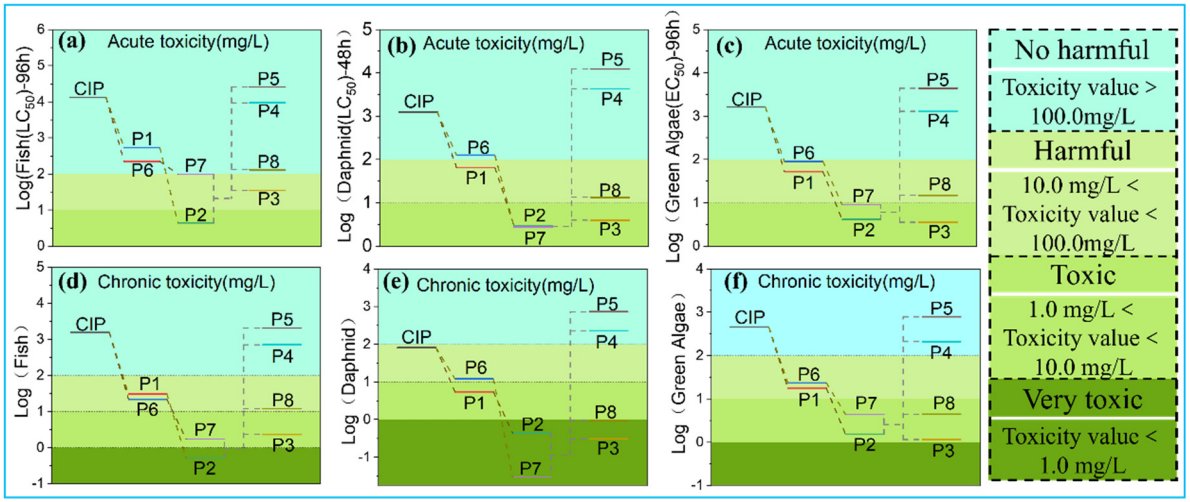

Figure 6. (**a**–**c**) Acute toxicity, (**d**–**f**) chronic toxicity for CIP and intermediates via the ECOSAR program.

To investigate the actual toxicity of CIP and degradation products to organisms, the effects on seed germination and seedling growth were also evaluated utilizing pea and wheat seeds. Figure 7a shows the schematic diagram of pea seedling growth, where groups A, B, and C were sprayed with deionized water, CIP solution, and CIP degradation residual solution, respectively. Figure 7b illustrates the optical images of pea seed germination and growth. Notably, within the growth period (12 days), the CIP solution (40 mg/L) strongly inhibited root and shoot elongation in seedlings. The inhibitory effects of low concentrations of CIP and its degradation products on seedlings gradually diminished as irradiation time increased. Furthermore, the growth patterns of seedlings treated with the degraded residual solution were similar to those of the blank control group. The seedling growth indexes were measured, as shown in Figure 7c,d. The germination rate of pea seedlings treated with the initial CIP solution reached 87%, with inhibition rates of 71.7% and 32.9% for shoot and root elongation, respectively. However, the inhibition rates for shoot and root elongation decreased to 4.4% and 14.7%, respectively, in the degraded residual solution. This indicated that photocatalytic treatment of CIP with $Bi_4Ti_3O_{12}$−24h significantly diminished the biotoxicity of the reaction solution toward pea seedlings under the tested conditions. Additionally, wheat seedling growth experiments verified this view, as shown in Figure 7e. The CIP molecule suppressed seedling growth by inhibiting cellular DNA replication and disrupting cell membrane structure [55]. Analysis of wheat seedlings' plant height and stem−leaf color revealed that seedlings treated with residual solution kept consistent with the water−treated group.

An animal toxicity experiment was conducted to evaluate CIP degradation residues using newly hatched zebrafish larvae. The developmental conditions of zebrafish larvae in various solutions are shown in Figure 8. In particular, the zebrafish larvae did not exhibit significant developmental differences (mortality or malformation rates) in acute toxicity tests (96 h) across various solutions. However, in the later stages of the experiment, some larvae exposed to CIP solution (40 mg/L) exhibited spinal curvature (SB) malformation, whereas no other malformations (e.g., yolk sac edema, eye malformation, tail bent) were observed in the remaining groups. The CIP solution showed a certain teratogenic risk to zebrafish larva, while the CIP solution after irradiation did not cause adverse effects on larval development within a short period. Comprehensively, even though partial degradation of CIP was achieved through $Bi_4Ti_3O_{12}$−24h photocatalytic treatment, under the experimental conditions, this process mitigated the biotoxicity of the CIP reaction solution toward several individual organisms, including plants and animals, probably due to antagonistic interactions between undegraded CIP molecules and toxic intermediates.

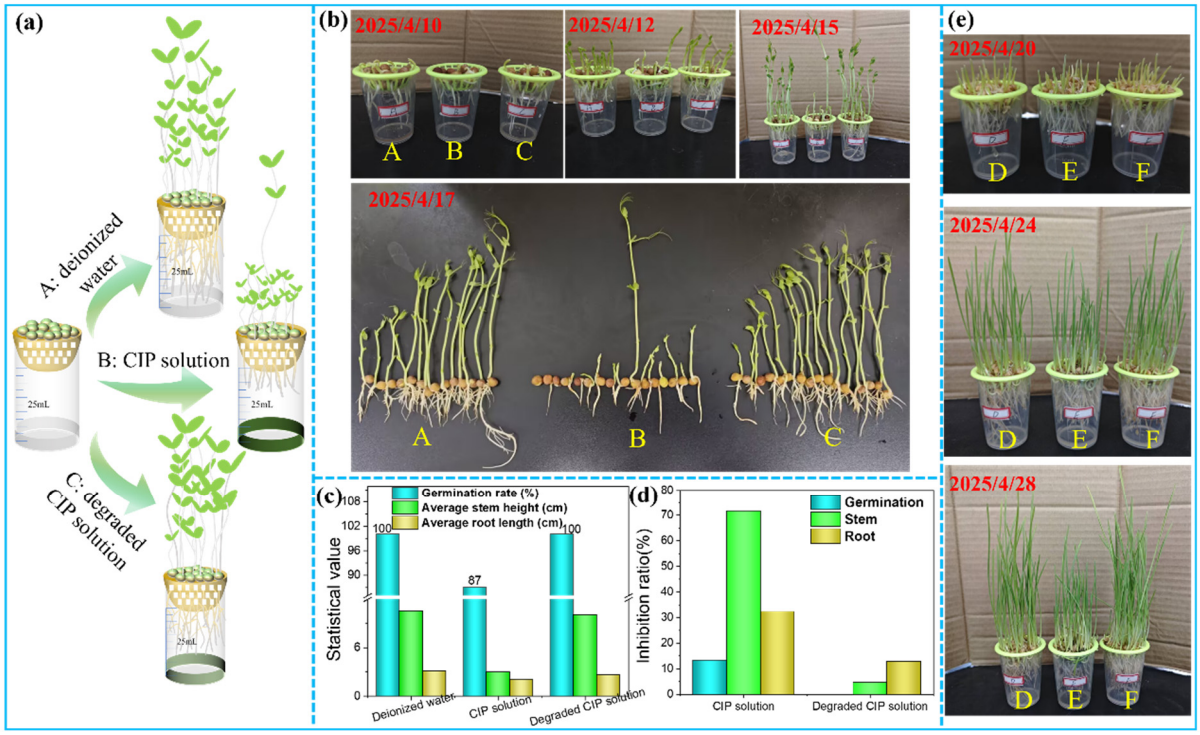

Figure 7. Schematic diagram (**a**) and optical image (**b**) of pea seedling growth; root and shoot elongation values (**c**) and inhibition rate (**d**) of seed germination for various solutions; optical image of wheat seedling growth (**e**), groups D, E, and F were sprayed with deionized water, CIP solution, and degradation residual solution, respectively.

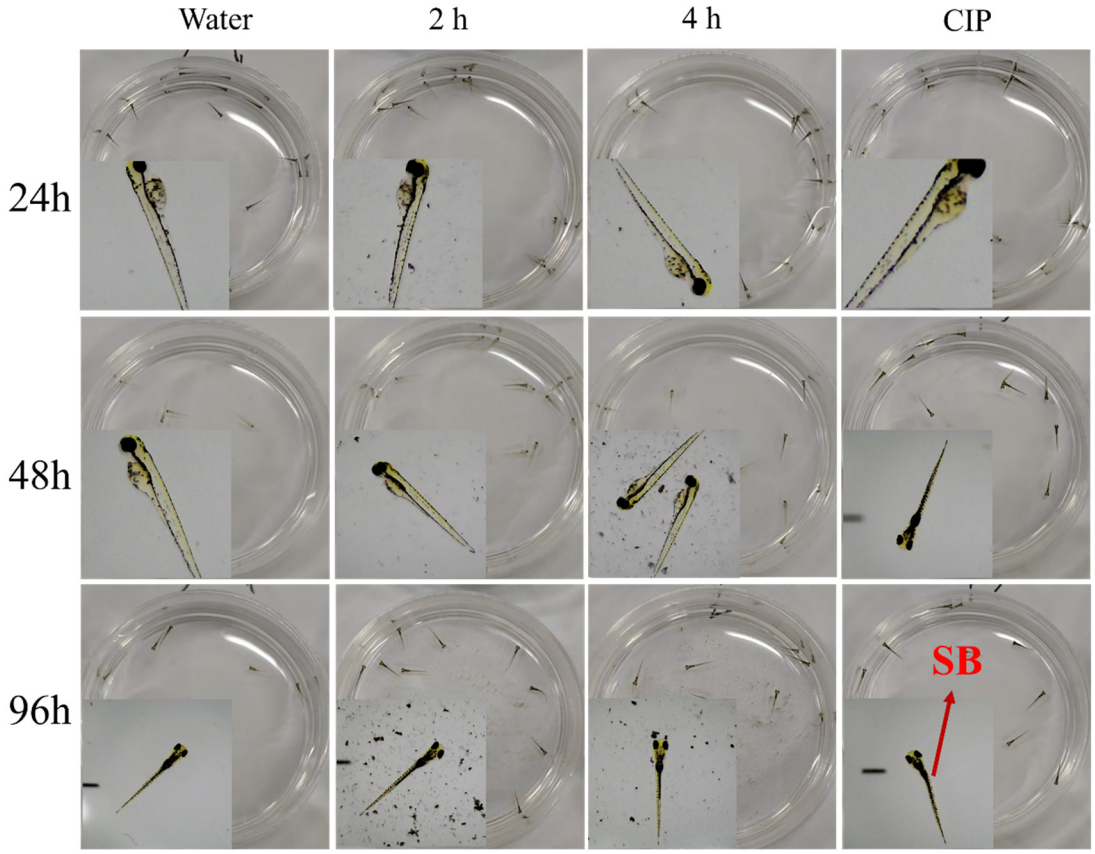

Figure 8. Optical images of zebrafish larvae in various solutions under the microscopy.

4. Conclusions

This study investigated $Bi_4Ti_3O_{12}$ nanosheets derived from $Na_2Ti_3O_7$ nanowires via ethylene glycol hydrothermal treatment, and analyzed the composition and surface morphology of the prepared materials. The photocatalytic activity for CIP degradation and the biotoxicity of the degradation residual solution were also performed. DRS and EPR characterization showed that hydrothermal treatment with ethylene glycol struggled to improve the photo−absorption range and surface oxygen vacancy concentration of $Bi_4Ti_3O_{12}$. However, photo/electrochemical characterization revealed a suitable ethylene glycol post−treatment duration could slightly optimize the separation behavior of photogenerated carriers in $Bi_4Ti_3O_{12}$ and expose more active sites, thereby enhancing photocatalytic performance. The ECOSAR model predicted that a little few degradation products may exhibit high toxicity to daphnia. Under the present experimental conditions, the CIP degradation residual solution would have no short−term effect on the growth and development of several actual individual organisms.

Supplementary Materials

The following supporting information can be found at: https://www.sciepublish.com/article/pii/1016, Figure S1: (a) Degradation curves and (b) kinetic curves of CIP with different catalysts; Figure S2: (a) Degradation curves and (b) kinetic curves of CIP with different catalysts; Figure S3: (a) Degradation curves and (b) kinetic curves of CIP with different catalysts; Figure S4: Cyclic voltammetric curve of $Bi_4Ti_3O_{12}$ (a), $Bi_4Ti_3O_{12}$−12h (b), $Bi_4Ti_3O_{12}$−24h (c), and $Bi_4Ti_3O_{12}$−36h (d); Figure S5: UV−DRS (a) and bandgap (b) of the sample $Bi_4Ti_3O_{12}$, $Bi_4Ti_3O_{12}$−12h, $Bi_4Ti_3O_{12}$−24h, and $Bi_4Ti_3O_{12}$−36h; Figure S6: EPR of the sample $Bi_4Ti_3O_{12}$, $Bi_4Ti_3O_{12}$−12h, $Bi_4Ti_3O_{12}$−24h, and $Bi_4Ti_3O_{12}$−36h; Figure S7: HRMS spectra at degradation times of (a) 30, (b) 120, and (c) 240 min; Table S1: A comparative study on photocatalytic degradation of CIP with different photocatalysts.

Acknowledgments

The authors would like to thank the Graduate Education Innovation Fund of Wuhan Institute of Technology (CX2024002).

Author Contributions

B.H.: Writing—original draft, Investigation, Formal analysis, Data curation. K.C.: Investigation, Data curation. J.W.: Investigation. G.C.: Writing—review & editing, Supervision, Project administration, Conceptualization.

Ethics Statement

This study did not involve human or animal subjects.

Informed Consent Statement

This study did not involve human participants and no informed consent was required.

Data Availability Statement

Data will be made available on request.

Funding

This research received no external funding.

Declaration of Competing Interest

The authors declare that they have no known competing financial interests or personal relationships that could have appeared to influence the work reported in this paper.

References

1. Yousefi M, Farzadkia M, Mahvi AH, Kermani M, Gholami M, Esrafili A. Photocatalytic degradation of ciprofloxacin using a novel carbohydrate−based nanocomposite from aqueous solutions. *Chemosphere* **2024**, *349*, 140972. DOI:10.1016/j.chemosphere.2023.140972
2. Yu G, Sun Q, Yang Y, Chen S, Long Y, Li Y, et al. BiOCl−based composites for photocatalytic degradation of antibiotics: A review of synthesis method, modification, factors affecting photodegradation and toxicity assessment. *J. Alloys Compd.* **2024**, *981*, 173733. DOI:10.1016/j.jallcom.2024.173733
3. Hayes A, Murray LM, Stanton IC, Zhang L, Snape J, Gaze WH, et al. Predicting selection for antimicrobial resistance in UK wastewater and aquatic environments: Ciprofloxacin poses a significant risk. *Environ. Int.* **2022**, *169*, 107488. DOI:10.1016/j.envint.2022.107488
4. Kim TK, Kim T, Park H, Lee I, Jo A, Choi K, et al. Degradation of ciprofloxacin and inactivation of ciprofloxacin resistant *E. faecium* during UV−LED (275 nm)/chlorine process. *Chem. Eng. J.* **2020**, *394*, 124803. DOI:10.1016/j.cej.2020.124803
5. Chen J, Zhu H, Ren Q, Chen S, Ding Y, Jin Z, et al. Efficient degradation of ciprofloxacin by Cu_2O/g−C_3N_4 heterostructures with different morphologies driven under the visible light. *Appl. Surf. Sci.* **2023**, *624*, 157186. DOI:10.1016/j.apsusc.2023.157186
6. Nie J, Yu X, Liu Z, Zhang J, Ma Y, Chen Y, et al. Energy band reconstruction mechanism of Cl−doped Cu_2O and photocatalytic degradation pathway for levofloxacin. *J. Clean. Prod.* **2022**, *363*, 132593. DOI:10.1016/j.jclepro.2022.132593
7. Wu Z, Liu J, Zhen L, Shi J, Deng H. Enhanced degradation of ciprofloxacin via Co−doped $Bi_2Fe_4O_9$ photocatalysis under peroxydisulfate activation. *Green Energy Environ.* **2025**, *10*, 1311–1325. DOI:10.1016/j.gee.2024.12.008
8. Cheng T, Ma Q, Gao H, Meng S, Lu Z, Wang S, et al. Enhanced photocatalytic activity, mechanism and potential application of I_{doped}−$Bi_4Ti_3O_{12}$ photocatalysts. *Mater. Today Chem.* **2022**, *23*, 100750. DOI:10.1016/j.mtchem.2021.100750
9. Zhang W, Zhao F, Han J, Wu J, Nie X, Wang Z, et al. Preparation of polyetherimide/Bi_2MoO_6 composite membrane by electrospinning and hydrothermal method for rapid photocatalysis and its degradation mechanism. *J. Water Process Eng.* **2025**, *78*, 108681. DOI:10.1016/j.jwpe.2025.108681
10. Lin Y−J, Wu F−Y, Wu Y, Xiao F−X. Single−atom alloys for photocatalytic applications: Material innovation and light−driven reactivity. *J. Mater. Chem. A* **2025**, *13*, 36056–36071. DOI:10.1039/D5TA04700E
11. Wu H−L, Liu J−W, Tan C−L, Tang Z−R. Dual−functional photoredox catalysis over Ni/CdS composite. *Mol. Catal.* **2026**, *592*, 115763. DOI:10.1016/j.mcat.2026.115763
12. Zhang Y, Tan C−L, Xu Y−J, Tang Z−R. Emerging platform and frontier of upcycling plastic waste by regulating photoredox half−reactions. *Mol. Catal.* **2026**, *588*, 115545. DOI:10.1016/j.mcat.2025.115545
13. Cheng Y, Yu T, Zheng C, Lei X, Li J, Liu X, et al. Bi nanoclusters construction and oxygen vacancy engineering for enhanced piezo−photocatalytic degradation performance of $BiVO_4$. *Chem. Eng. J.* **2025**, *522*, 167714. DOI:10.1016/j.cej.2025.167714
14. Liu J, Chang X, Cheng Y, Guo Z, Yan Q. Construction of novel Ag/AgI/$Bi_4Ti_3O_{12}$ plasmonic heterojunction: A study focusing on the performance and mechanism of photocatalytic removal of tetracycline. *Chemosphere* **2024**, *352*, 141306. DOI:10.1016/j.chemosphere.2024.141306
15. Song S, Meng Z, Du A, Liu P, Li K, Zhang X, et al. *In situ* constructed Bi/BiOBr nanoflower for synergistic H_2O_2 generation and pollutant degradation: Coupling built−in electric field with SPR effect and environmental risk assessment. *J. Mater. Chem. A* **2025**, *13*, 31684–31698. DOI:10.1039/D5TA05840F
16. Nannou C, Maroulas KN, Tsamtzidou C, Ladomenou K, Kyzas GZ. Photocatalytic degradation of veterinary antibiotics in wastewaters: A review. *Sci. Total Environ.* **2025**, *966*, 178765. DOI:10.1016/j.scitotenv.2025.178765
17. Li C, Tian Q, Zhang Y, Li Y, Yang X, Zheng H, et al. Sequential combination of photocatalysis and microalgae technology for promoting the degradation and detoxification of typical antibiotics. *Water Res.* **2022**, *210*, 117985. DOI:10.1016/j.watres.2021.117985
18. Tošić M, Savić J, Šobot AV, Živković S, Dimitrijević A, Ilić N, et al. Photocatalytic Degradation of Carbofuran in Water Using Laser−Treated TiO_2: Parameters Influence Study, Cyto− and Phytotoxicity Assessment. *Toxics* **2024**, *12*, 566. DOI:10.3390/toxics12080566

19. Cui Y, Yuan P, Liu W, Wang Z, Pal S, Briscoe J. A piezo−self−Fenton system based on dual co−catalyst modified $Bi_4Ti_3O_{12}$ with accelerated Fe^{3+}/Fe^{2+} cycle and efficient in situ production of H_2O_2. *J. Mater. Chem. A* **2025**, *13*, 3922–3934. DOI:10.1039/D4TA07694J
20. Supriya S. Tailoring layered structure of bismuth−based aurivillius perovskites: Recent advances and future aspects. *Coord. Chem. Rev.* **2023**, *479*, 215010. DOI:10.1016/j.ccr.2022.215010
21. Hailili R, Li Z. Synergizing photocatalysis with Aurivillius−phase $Bi_4Ti_3O_{12}$: Current insights and emerging trends. *J. Mater. Chem. A* **2025**, *13*, 16345–16381. DOI:10.1039/D4TA07986H
22. Liao L, Jiang Y, Gao Y, Guo L, Li M, Wang S, et al. Built−in electric field mediated efficient charge separation in Bi_x−$Bi_{(4-x)}Ti_3O_{12}$ nanosheets assembled hollow sphere photocatalyst. *Fuel* **2025**, *385*, 134020. DOI:10.1016/j.fuel.2024.134020
23. Ji B, Li X, Gao S, Qin Z, Wang C, Wang Q, et al. Polarization−enhanced piezo−photocatalysis over hollow−sphere $Bi_4Ti_3O_{12}$: Structure−property relationship and degradation mechanism. *Chin. J. Catal.* **2025**, *76*, 133–145. DOI:10.1016/S1872−2067(25)64758−9
24. Han M, Guo B, Zhang Z, Hu X, Wang Z. Hollow $Bi_4Ti_3O_{12}/TiO_2$ nanocakes for photocatalytic hydrogen generation. *J. Alloys Compd.* **2023**, *963*, 171192. DOI:10.1016/j.jallcom.2023.171192
25. Shi Y, Shen M, Wang Z, Liu C, Bi J, Wu L. Visible−light−driven benzyl alcohol oxidation over Pt/Mn−$Bi_4Ti_3O_{12}$ nanosheets: Structure−function relationship of multicomponent photocatalysts. *J. Catal.* **2023**, *418*, 141–150. DOI:10.1016/j.jcat.2023.01.015
26. Cheng T, Gao H, Wang S, Yi Z, Liu G, Pu Z, et al. Surface doping of $Bi_4Ti_3O_{12}$ with S: Enhanced photocatalytic activity, mechanism and potential photodegradation application. *Mater. Res. Bull.* **2022**, *149*, 111711. DOI:10.1016/j.materresbull.2021.111711
27. Liu Z, An Y, Zhang W, Zhu L, Zhu G. Au nanoparticles modified oxygen−vacancies−rich $Bi_4Ti_3O_{12}$ heterojunction for efficient photocatalytic NO removal with high selectivity. *J. Alloys Compd.* **2023**, *942*, 169018. DOI:10.1016/j.jallcom.2023.169018
28. Wan P, Hood ZD, Adhikari SP, Xu Y, Yang S, Wu S. Enhancing the photoresponse and photocatalytic properties of TiO_2 by controllably tuning defects across {101} facets. *Appl. Surf. Sci.* **2018**, *434*, 711–716. DOI:10.1016/j.apsusc.2017.11.003
29. Gao J, Xue J, Jia S, Shen Q, Zhang X, Jia H, et al. Self−Doping Surface Oxygen Vacancy−Induced Lattice Strains for Enhancing Visible Light−Driven Photocatalytic H_2 Evolution over Black TiO_2. *ACS Appl. Mater. Interfaces* **2021**, *13*, 18758–18771. DOI:10.1021/acsami.1c01101
30. Xu Y, Wang G, Yang B, Li Y, Chen L, Wang R, et al. La−doped $Bi_4Ti_3O_{12}$ nanosheets: Ferroelectric polarization−enhanced carrier dynamics for efficient tetracycline photodegradation. *J. Adv. Ceram.* **2026**, *15*, 9221248. DOI:10.26599/JAC.2026.9221248
31. Wu J, Qin N, Lin E, Yuan B, Kang Z, Bao D. Synthesis of $Bi_4Ti_3O_{12}$ decussated nanoplates with enhanced piezocatalytic activity. *Nanoscale* **2019**, *11*, 21128–21136. DOI:10.1039/C9NR07544E
32. Zhang Y, Gao J, Chen Z, Lu Z. Enhanced photocatalytic performance of $Bi_4Ti_3O_{12}$ nanosheets synthesized by a self−catalyzed fast reaction process. *Ceram. Int.* **2018**, *44*, 23014–23023. DOI:10.1039/C9NR07544E
33. Zhou H, Jiang S, Wang X, Zhi X, Zhang Z, Li X, et al. Polydopamine−modified g−C_3N_4/TiO_2/GO PVDF membranes for enhanced quinolone antibiotic photocatalytic removal. *J. Water Process Eng.* **2025**, *76*, 108280. DOI:10.1016/j.jwpe.2025.108280
34. Liu X, Bi RX, Yu FT, Zhang CR, Luo QX, Liang RP, et al. D−π−A array structure of $Bi_4Ti_3O_{12}$−triazine−aldehyde group benzene skeleton for enhanced photocatalytic uranium (VI) reduction. *J. Hazard. Mater.* **2023**, *451*, 131189. DOI:10.1016/j.jhazmat.2023.131189
35. He Y, Lv T, Zhou T, Liu B, Xiao B, Zheng H, et al. Cu doping enhanced $ZnIn_2S_4/TiO_2(V_O)$ Z−scheme heterojunction for efficient photocatalytic overall water splitting. *Int. J. Hydrogen Energy* **2024**, *57*, 491–499. DOI:10.1016/j.ijhydene.2024.01.037
36. Zha Y, He X, Wang Y, Chen W, Chen L, Chen L, et al. Visible−light−response Fe−doped BiOCl microspheres with efficient photocatalysis−Fenton degradation of antibiotics. *J. Water Process Eng.* **2024**, *67*, 106225. DOI:10.1016/j.jwpe.2024.106225
37. Zhao T, Hu J, Zhang W, Cheng G, Li W, Xiong J. Oxygen vacancy/metallic sites synergically assists hollow TiO_2–induced CO_2 photoreduction: Categories and roles. *Fuel* **2025**, *385*, 134107. DOI:10.1016/j.fuel.2024.134107
38. Ma B, Zha Y, Xu R, Li J, Guo Y, Liu J, et al. Hollow α−Bi_2O_3/TiO_2 nanotube arrays hierarchical heterojunction with strong interface interaction for efficient photocatalytic ciprofloxacin degradation. *J. Water Process Eng.* **2024**, *60*, 105134. DOI:10.1016/j.jwpe.2024.105134

39. Liu X, Zhang Y, Zhang W, Cheng G, Tian F, Li W, et al. Type II/Schottky heterojunctions−triggered multi−channels charge transfer in Pd−TiO_2−Cu_2O hybrid promotes photocatalytic hydrogen production. *J. Colloid Interface Sci.* **2025**, *685*, 173–185. DOI:10.1016/j.jcis.2025.01.091
40. Li XL, Yang GQ, Li SS, Xiao N, Li N, Gao YQ, et al. Novel dual co−catalysts decorated Au@HCS@PdS hybrids with spatially separated charge carriers and enhanced photocatalytic hydrogen evolution activity. *Chem. Eng. J.* **2020**, *379*, 122350. DOI:10.1016/j.cej.2019.122350
41. Liu X, Zhang Y, Zhang W, Cheng G, Tian F, Li W, et al. Oxidation cocatalyst/S−scheme junction cooperatively assists photocatalytic H_2 production in ternary hybrid: The case of PdO@TiO_2−Cu_2O. *Sep. Purif. Technol.* **2025**, *354*, 129396. DOI:10.1016/j.seppur.2024.129396
42. Hu B, Xiao M, Liu C, Che G, Jia J, Yan L, et al. Fabricate dual interface build−in electric fields by introducing Au nanospecies into Z−scheme heterojunction to propel photocatalytic CO_2 reduction. *Sep. Purif. Technol.* **2023**, *315*, 123726. DOI:10.1016/j.seppur.2023.123726
43. Gao W, Li G, Wang Q, Zhang L, Wang K, Pang S, et al. Ultrathin porous Bi_2WO_6 with rich oxygen vacancies for promoted adsorption−photocatalytic tetracycline degradation. *Chem. Eng. J.* **2023**, *464*, 142694. DOI:10.1016/j.cej.2023.142694
44. Amari A, Sultan Aljibori HS, Elboughdiri N, Algarni Z, Ismail MA, Kadhum AAH, et al. Synthesis of a highly efficient ternary Heterostructure for synergistic charge migration: Dual−functional enhancement in photocatalytic ciprofloxacin degradation and hydrogen production. *J. Water Process Eng.* **2024**, *65*, 105841. DOI:10.1016/j.jwpe.2024.105841
45. Wang Z, Cai X, Xie X, Li S, Zhang X, Wang Z. Visible−LED−light−driven photocatalytic degradation of ofloxacin and ciprofloxacin by magnetic biochar modified flower−like Bi_2WO_6: The synergistic effects, mechanism insights and degradation pathways. *Sci. Total Environ.* **2021**, *764*, 142879. DOI:10.1016/j.scitotenv.2020.142879
46. Dhanka AK, Kohlrausch EC, Samantray R, Kumar V, Pani B, Agasti N. Harnessing defects in Ag/CeO_2 for enhanced photocatalytic degradation of antibiotic in water: Structural characteristics, in−depth insights on mechanism, degradation pathway. *Chem. Eng. J. Adv.* **2025**, *21*, 100706. DOI:10.1016/j.ceja.2025.100706
47. Harini G, Okla MK, Alaraidh IA, Mohebaldin A, Al−ghamdi AA, Abdel−Maksoud MA, et al. Sunlit expeditious visible light−mediated photo−fenton degradation of ciprofloxacin by exfoliation of $NiCo_2O_4$ and $Zn_{0.3}Fe_{2.7}O_4$ over g−C_3N_4 matrix: A brief insight on degradation mechanism, degraded product toxicity, and genotoxic evaluation in Allium cepa. *Chemosphere* **2022**, *303*, 134963. DOI:10.1016/j.chemosphere.2022.134963
48. Hu X, Hu X, Peng Q, Zhou L, Tan X, Jiang L, et al. Mechanisms underlying the photocatalytic degradation pathway of ciprofloxacin with heterogeneous TiO_2. *Chem. Eng. J.* **2020**, *380*, 122366. DOI:10.1016/j.cej.2019.122366
49. Xing X, Du Z, Zhuang J, Wang D. Removal of ciprofloxacin from water by nitrogen doped TiO_2 immobilized on glass spheres: Rapid screening of degradation products. *J. Photochem. Photobiol. A Chem.* **2018**, *359*, 23–32. DOI:10.1016/j.jphotochem.2018.03.026
50. He R, Xue K, Wang J, Yan Y, Peng Y, Yang T, et al. Nitrogen−deficient g−C_3N_x/POM_s porous nanosheets with P–N heterojunctions capable of the efficient photocatalytic degradation of ciprofloxacin. *Chemosphere* **2020**, *259*, 127465. DOI:10.1016/j.chemosphere.2020.127465
51. Tripathy SP, Subudhi S, Ray A, Behera P, Bhaumik A, Parida K. Mixed−Valence bimetallic Ce/Zr MOF−Based nanoarchitecture: A visible−light−active photocatalyst for ciprofloxacin degradation and hydrogen evolution. *Langmuir* **2022**, *38*, 1766–1780. DOI:10.1021/acs.langmuir.1c02873
52. Ji Q, Cheng X, Wu Y, Xiang W, He H, Xu Z, et al. Visible light absorption by perylene diimide for synergistic persulfate activation towards efficient photodegradation of bisphenol A. *Appl. Catal. B Environ. Energy* **2021**, *282*, 119579. DOI:10.1016/j.apcatb.2020.119579
53. Zhang H, Quan H, Yin S, Sun L, Lu H. Unraveling the toxicity associated with ciprofloxacin biodegradation in biological wastewater treatment. *Environ. Sci. Technol.* **2022**, *56*, 15941–15952. DOI:10.1021/acs.est.2c04387
54. Wang Y, Zhou T, Chen D, Zhang Z−X, Zhang Q, Ye X, et al. Fenton−like catalysis by MnO_2 membrane reactor with oxygen vacancies for carbamazepine degradation. *Appl. Catal. B Environ. Energy* **2024**, *353*, 124106. DOI:10.1016/j.apcatb.2024.124106
55. Sharma M, Rajput D, Kumar V, Jatain I, Aminabhavi TM, Mohanakrishna G, et al. Photocatalytic degradation of four emerging antibiotic contaminants and toxicity assessment in wastewater: A comprehensive study. *Environ. Res.* **2023**, *231*, 116132. DOI:10.1016/j.envres.2023.116132